SciPost Physics Submission

Tachyonic and parametric instabilities in an extended bosonic Josephson junction

Laura Batini[1]⋆, Sebastian Erne[2]†, Jörg Schmiedmayer[2], and Jürgen Berges[1]

1 Institut für Theoretische Physik, Universität Heidelberg, Philosophenweg 16, 69120 Heidelberg, Germany
2 Vienna Center for Quantum Science and Technology, Atominstitut, TU Wien, Stadionallee 2, 1020 Vienna, Austria

⋆ batini@thphys.uni-heidelberg.de , † sebastian.erne@tuwien.ac.at

Abstract

We study the decay of phase coherence in an extended bosonic Josephson junction realized via two tunnel-coupled Bose-Einstein condensates. Specifically, we focus on the π-trapped state of large population and phase imbalance, which, similar to the breakdown of macroscopic quantum self-trapping, becomes dynamically unstable due to the amplification of quantum fluctuations. We analytically identify early tachyonic and parametric instabilities connected to the excitation of atom pairs from the condensate to higher momentum modes along the extended direction. Furthermore, we perform Truncated Wigner numerical simulations to observe the build-up of non-linearities at later times and explore realistic experimental parameters.

Received Date
Accepted Date
Published Date

Contents

---

1 Introduction

Quantum phase coherence is a central ingredient for macroscopic quantum phenomena in fundamental physics or technological applications and an important resource in quantum computation [1]. A clear manifestation of macroscopic quantum phase coherence is the Josephson effect based on quantum tunneling through a potential barrier between two superconductors or superfluids [2, 3]. Ultracold atomic gases are particularly versatile platforms for studying these phenomena [4–6]. They provide exceptional control over system parameters and advanced imaging techniques to monitor even detailed out-of-equilibrium properties.

Already, the dynamics of the zero-dimensional (0D) Josephson junction [7] is very rich and depends on whether the atom-atom interaction energy or the tunneling energy dominates, as well as the total energy of the system [4, 8, 9]. Depending on those parameters, the system may only allow a fraction of atoms to tunnel back and forth between two wires, resulting in an unbalanced state, corresponding to a nonzero average population difference, as opposed to Josephson oscillations [6, 10, 11]. Additionally, when the state is unbalanced, the relative phase between the two condensates can either monotonically increase in time, corresponding to a running phase, which defines the macroscopic quantum self-trapping (MQST) [12], or be trapped, oscillating close to π, referred to as the π-mode, or π-oscillation [13].

Transitioning from the zero-dimensional to an extended bosonic Josephson junction, the multimode nature of the extended direction leads to further interesting physics [14–18]. In fact, due to the extended spatial direction, the system hosts a number of different instabilities absent in 0D.

While in the Josephson regime, there are several theoretical [19–27] and experimental [7, 17, 18, 28–32] studies, the stability of the MQST and π-state is far less explored. In the regime of MQST, it was predicted theoretically that the state becomes dynamically unstable due to the appearance of non-trivial scattering solutions related to the emission of correlated pairs of excitations [33]. One promising experimental setup is provided by two parallel weakly-coupled elongated Bose-Einstein condensates (BECs) [14–18]. While the decay of strongly imbalanced condensates has been observed [29, 30], a detailed comparison to theoretical predictions was hindered by the harmonic confinement. The π-state was experimentally observed in a superfluid ^{3}He weak link [34], but an experimental realization in a BEC system is not yet known. Moreover, a comprehensive microscopic understanding of the origin of the breakdown in the π-trapped regime has not yet been explored.

In this work, we provide a theoretical analysis of the out-of-equilibrium dynamics of the π-mode. After reviewing the stable mean-field dynamics, we focus first on the effect of fluctuations on the linearized level, destabilizing the state. We perform an analytical study of the excited modes and their respective growth rates. One can distinguish primary instabilities

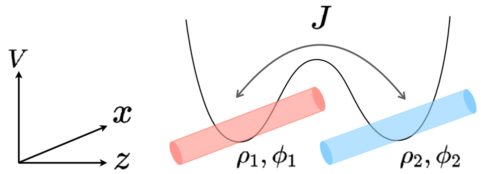

Figure 1: Sketch of the experimental setup under study, consisting of two elongated condensates (left 1 and right 2). The BECs are characterized by an atomic density $\rho_{1,2}$ and a phase $\phi_{1,2}$. The BECs are coupled by a single-particle tunnel interaction J.

where the growth of characteristic modes is shown to be of tachyonic and parametric resonance origin [35–37]. To go beyond the linearized analysis, we compare with the numerical results obtained from simulations using a Truncated Wigner Approximation (TWA) [38]. This allows us to identify secondary instabilities [35,36], which represent the even faster non-linear growth of modes triggered by the primary instabilities [35, 36]. Our study provides the basis for quantitative comparisons with future experimental implementations.

This paper is organized as follows. In Sec. 2, we introduce the theoretical model and the dynamical regime of the π-mode. In Sec. 3, we analyze the early dynamics of this many-body system, focusing on the instability chart for the primary instabilities. In the following section 4, we demonstrate numerically the existence of secondaries being present in this system and discuss their generation. We also relate to possible experimental realizations. Finally, Sec. 5 concludes and gives an outlook. The appendices provide a brief review of the mean-field picture and information on the implementation of the numerical classical-statistical simulations.

2 Tunnel-coupled Bose condensates

We consider a system of two weakly tunnel-coupled elongated BECs, which are trapped in a double-well potential [39, 40]. This section summarizes the theoretical model and derives the relevant equations for the π-state using a density-phase representation. For a more detailed discussion on the experimental implementation and feasibility, we refer to Sec. 4.1.

2.1 Model and equations of motion

The system under consideration comprises two quasi-1D Bose gases, each trapped in one well of a double-well potential, as depicted in Fig. 1. They are described by the following Hamiltonian [26]

$$\hat{H} = \int_0^L \mathrm{d}x \left\{ \frac{-\hbar^2}{2m} \left(\hat{\Psi}_1^\dagger \partial_x^2 \hat{\Psi}_1 + \hat{\Psi}_2^\dagger \partial_x^2 \hat{\Psi}_2 \right) + \frac{g}{2} \left[(\hat{\Psi}_1^\dagger \hat{\Psi}_1)^2 + (\hat{\Psi}_2^\dagger \hat{\Psi}_2)^2 \right] - \hbar J (\hat{\Psi}_1^\dagger \hat{\Psi}_2 + \hat{\Psi}_2^\dagger \hat{\Psi}_1) \right\}. \tag{1}$$

Here L is the system size, m is the atom mass, and $\hat{\Psi}_j(t,x)$ for $j = 1,2$ represents the bosonic field operator, which obeys the canonical equal-time commutation relations

$$\begin{aligned} \left[\hat{\Psi}_i(t,x), \hat{\Psi}_j(t,x') \right] &= \left[\hat{\Psi}_i^\dagger(t,x), \hat{\Psi}_j^\dagger(t,x') \right] = 0, \\ \left[\hat{\Psi}_i(t,x), \hat{\Psi}_j^\dagger(t,x') \right] &= \hbar \delta_{ij} \delta(x - x'), \end{aligned} \tag{2}$$

with $i, j = 1,2$. The first line in Eq. (1) contains the free part of the Hamiltonian, which includes the kinetic term. In the second line, the term $\sim g$ is the interaction term, and the hopping term $\sim J$ characterizes the tunneling strength between the two systems, which is determined from the overlap integrals of the radial wave function. Due to the spatial separation of the two condensates, intra-species interactions are considered to be negligible.

2.2 Equations of motion

The coupled evolution equations for the 2-component BEC follow from the Heisenberg equations of motion derived from the Hamiltonian in Eq. (1),

$$i\hbar\frac{\partial}{\partial t}\hat{\Psi}_1 = -[\hat{H},\hat{\Psi}_1] = \left(-\frac{\hbar^2\partial_x^2}{2m} + g|\hat{\Psi}_1|^2\right)\hat{\Psi}_1 - \hbar J\hat{\Psi}_2, \tag{3}$$

and similarly for $\hat{\Psi}_2$ by replacing $\hat{\Psi}_1 \longleftrightarrow \hat{\Psi}_2$ in Eq. (3).

In order to study the quantum dynamics approximately, we adopt a semi-classical perspective. Specifically, we consider the Gross-Pitaevskii equations (GPEs) of motion that are obtained after replacing the Bose field operator in Eq. (3) by a corresponding classical field with $\hat{\Psi}_j(t,x) \to \Psi_j(t,x)$. In the semi-classical description, the statistical averages of the classical fields have to fulfill the same initial conditions at a given time t_0 as the quantum fields for the quantum expectation values of their means, $\langle\hat{\Psi}_j(t_0,x)\rangle$, and their fluctuations encoded in two-point correlations, $\langle\hat{\Psi}_j(t_0,x)\hat{\Psi}_k(t_0,y)\rangle$ or also higher correlations, which are suitably symmetrized to describe the equal initial times. The semi-classical approach is particularly useful to derive the linearized evolution equations for fluctuations below and for the non-linear TWA description of Sec. 4. For more details, we refer to Appendix B.

Furthermore, it is convenient to consider the Madelung representation, where the fields $\Psi_j(t,x)$ for $j = 1,2$ are expressed in terms of the condensate densities $\rho_j(t,x)$ and phases $\phi_j(t,x)$, such that

$$\Psi_j = \sqrt{\rho_j}\, e^{i\phi_j}\, . \tag{4}$$

In terms of these variables the coupled GPEs become for the densities and phases

$$\begin{aligned}
\hbar\dot{\rho}_1 &= -\frac{\hbar^2}{m}\left(\rho_1\partial_x^2\phi_1 + \partial_x\rho_1\cdot\partial_x\phi_1\right) - 2\hbar J\sqrt{\rho_1\rho_2}\,\sin(\phi_2-\phi_1),\\
\hbar\dot{\phi}_1 &= \frac{\hbar^2}{2m}\left(\frac{\partial_x^2\rho_1}{2\rho_1} - \frac{(\partial_x\rho_1)^2}{4\rho_1^2} - (\partial_x\phi_1)^2\right) - g\rho_1 + \hbar J\sqrt{\frac{\rho_2}{\rho_1}}\cos(\phi_2-\phi_1),
\end{aligned} \tag{5}$$

respectively and correspondingly for ρ_2 and ϕ_2. Here, $\dot{\rho}_j \equiv \partial\rho_j/\partial t$, and equivalently for ϕ_j, denotes the derivative with respect to time. It is convenient to define the relative degrees of freedom, $z \equiv (\rho_1-\rho_2)/(\rho_1+\rho_2)$, with $-1 < z < 1$, and the relative phase $\phi \equiv \phi_1 - \phi_2$.

2.3 Two-mode approximation

We first consider the mean field evolution of a purely homogeneous background field configuration such that $\rho_j(x,t) = \bar{\rho}_j(t), \phi_j(x,t) = \bar{\phi}_j(t)$. In terms of the mean field relative imbalance $\bar{z}$ and phase $\bar{\phi}$ they are given by

$$\begin{aligned}
\hbar\dot{\bar{z}}(t) &= -2\hbar J\sqrt{1-\bar{z}^2(t)}\sin\bar{\phi}(t),\\
\hbar\dot{\bar{\phi}}(t) &= \hbar J\left[\Lambda\bar{z}(t) + \frac{2\bar{z}(t)}{\sqrt{1-\bar{z}^2(t)}}\cos\bar{\phi}(t)\right],
\end{aligned} \tag{6}$$

which are invariant under discrete shift symmetry $\bar{\phi} \to \bar{\phi} + 2\pi l$, $l \in \mathbb{N}$. We refer to Ref. [13] and Appendix A for details of the derivation. In Eq. (6), the dimensionless parameter Λ, defined by

$$\Lambda \equiv \frac{\mu}{\hbar J}, \tag{7}$$

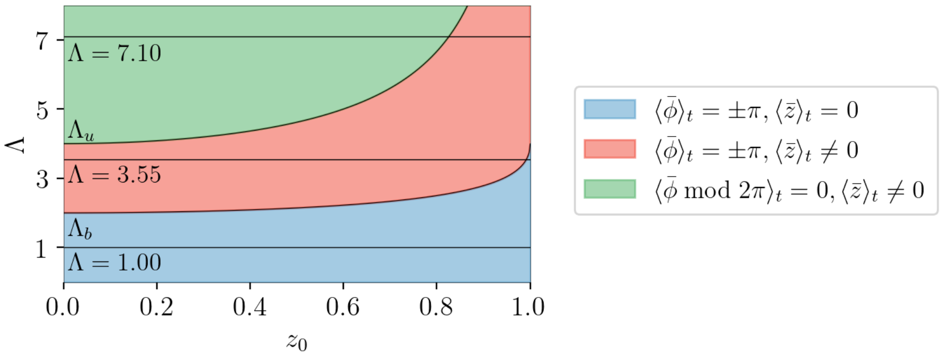

Figure 2: Parameter space (Λ, z_0) showing the dynamical regimes delineated by Λ_b [Eq. (9)] and Λ_u [Eq. (10)], for an initial phase difference of $\phi_0 = \pi$. The horizontal lines represent $\Lambda = \{1.00, 3.55, 7.10\}$.

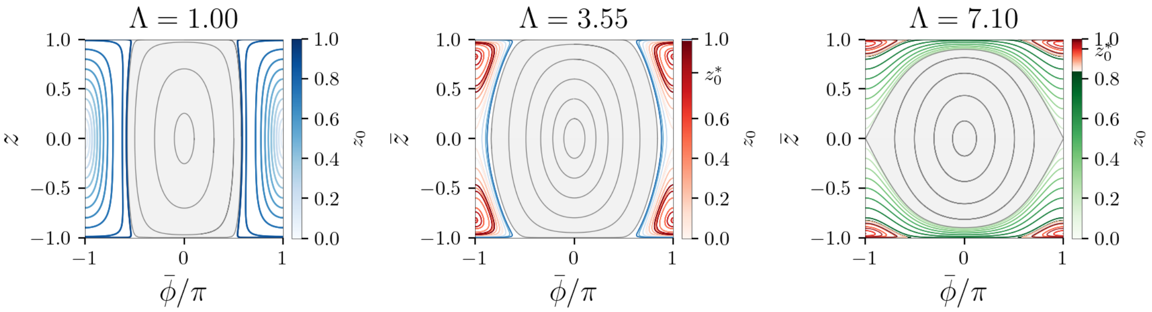

Figure 3: The dynamics of the mean fields $\bar{\phi}$ and $\bar{z}$ corresponding to Fig. 2. For $\Lambda < \Lambda_b(z_0)$, the system exhibits π_0-oscillations, characterized by $\langle\bar{\phi}\rangle_t = \pi, \langle\bar{z}\rangle_t = 0$ as visible in the left and center panels. For $\Lambda_b(z_0) < \Lambda < \Lambda_u(z_0)$, the system displays π-oscillations, where $\langle\bar{\phi}\rangle_t = \pi, \langle\bar{z}\rangle_t \neq 0$ as visible in the center and right panels (blue lines). For $\Lambda > \Lambda_u(z_0)$, the system exhibits MQST self-trapped modes, characterized by $\langle\bar{\phi}\rangle_t = 0, \langle\bar{z}\rangle_t \neq 0$ and it is shown in the right plot (green lines). In all plots, the gradient bar indicates the initial condition for z_0.

characterizes the ratio between the interatomic interaction and the tunneling energies, $\mu_j = \rho_j g$ is the chemical potential in each well, and $\mu = \mu_1 + \mu_2$ denotes the total chemical potential. In this work, we consider repulsive interatomic interactions, such that g and Λ are always positive.

2.3.1 Dynamical regimes

The system exhibits a range of different behaviors for various initial conditions. The dynamical modes are fully determined by the initial conditions (ϕ_0, z_0) and the dimensionless parameter Λ. In the following, we focus our discussion on the π-state dynamics and, therefore, without loss of generality, fix the initial condition for the relative phase to $\phi_0 = \pi$[1]. The different possible dynamical regimes are conveniently represented in parameter space (Λ, z_0) [30], which are illustrated in Fig. 2. Let us review the three qualitatively different regimes for a fixed initial condition for z_0.

- (Only) phase trapping, occurring for $\Lambda < \Lambda_b(z_0)$. The dynamics in this regime presents slightly deformed oscillations of the imbalance, such that $\langle\bar{z}\rangle_t = 0$. The expression $\langle\ldots\rangle_t$

---

[1] It is important to note that the commonly discussed Josephson oscillation regime is excluded due to the initial condition choice of $\phi_0 = \pi$. We have indicated this regime with the gray shaded area in Fig. 2.

indicates the temporal average. The relative phase is trapped around π, i.e., $\langle\bar{\phi}\rangle_t = \pm\pi$. This phenomenon is called π_0-*oscillations* and is shown in the left panel of Fig. 3.

- Phase *and* density trapping, occurring for $\Lambda \in (\Lambda_b, \Lambda_u)$. This phenomenon is known as the π-*oscillations*. In this case, $\langle\bar{\phi}\rangle_t = \pm\pi$ and $\langle\bar{z}\rangle_t \neq 0$. As shown in the central and right panels of Fig. 3, the imbalance oscillations are centered around one of the four limiting points $\pm z_0^*$, where the amplitude of the oscillations drops to zero. Analytically, these points are located at [30]

$$(\bar{\phi}, \bar{z}) = \left(\pm\pi, \pm\sqrt{1 - \frac{4}{\Lambda^2}}\right). \tag{8}$$

In order to observe the π-oscillations, it is essential to carefully choose the initial condition z_0 (or Λ). The lower bound Λ_b is determined by the initial imbalance z_0. It arises from the requirement that the effective potential for the imbalance (see Appendix A.2 and, in particular, Eq. (A.7) for more details) must be in the symmetry-broken phase to ensure that the imbalance remains trapped at all times. Additionally, the total energy must be negative to prevent the imbalance from surpassing the potential barrier. This energy condition is even more stringent, as discussed in Refs. [33, 41], and gives

$$\Lambda_b = \frac{4\left(1 - \sqrt{1 - z_0^2}\right)}{z_0^2}. \tag{9}$$

The upper bound Λ_u amounts to

$$\Lambda_u = \frac{4}{\sqrt{1 - z_0^2}}. \tag{10}$$

This bound results from the condition that the phase remains trapped at all times.

- (Only) imbalance trapping, occurring for $\Lambda > \Lambda_u$. This regime corresponds to *macroscopic quantum self-trapping (MQST)*, characterized by $\langle\bar{z}\rangle_t \neq 0$ and the circular mean of the relative phase given by $\langle\bar{\phi} \mod 2\pi\rangle_t = 0$. The corresponding time evolution of the mean fields is shown in the right panel of Fig. 3.

In this work, unless stated otherwise, we set $\Lambda = 3.55$. This value ensures that, for nearly all initial values of z_0, the system remains in the π-trapped regime [see Fig. 2]. At the same time, it places the system close to the perturbative regime in the coupling $(1/\Lambda \ll 1)$.

3 Instabilities from linearized fluctuation equations

In this section, we investigate the stability of the mean-field trajectories when transitioning from the 0D bosonic Josephson junction to an extended junction. Here, we focus on the breakdown of the π-oscillations. In general, the extended direction enables the decay of this state through the excitation of correlated pairs of atoms, energetically prohibited in 0D.

At short times, when the occupation of the non-condensate modes are small, we linearize the equations of motion in the fluctuations around the previously discussed mean fields $\bar{\rho}_j$ and $\bar{\phi}_j$, which allows us to obtain analytical predictions of the instability bands in different regimes.

We characterize the instabilities by their dispersion relations. In particular, the non-zero imaginary components lead to their exponential growth. First, we consider the simple case where the relative phase and the density of the condensates are initialized at a mean-field stationary point. Then, we extend the calculation of the linearized evolution to more general cases, considering the presence of oscillations around the mean-field stable point. In this case, parametric oscillations lead to further instability bands.

3.1 Exponential amplification of fluctuations

We write each condensate density ρ_j and phase ϕ_j in terms of their homogeneous means $\bar{\rho}_j(t)$ and $\bar{\phi}_j(t)$, with small fluctuations $\delta\rho_j(t,x)$ and $\delta\phi_j(t,x)$ on top as

$$\begin{aligned} \rho_j(t,x) &= \bar{\rho}_j(t) + \delta\rho_j(t,x), \\ \phi_j(t,x) &= \bar{\phi}_j(t) + \delta\phi_j(t,x). \end{aligned} \tag{11}$$

Linearizing Eq. (5), we recover to zeroth order in the phase and density fluctuations the mean-field equations corresponding to Eq. (6). To linear order in the fluctuations, the following equations are obtained [42, 43]:

$$\begin{aligned} \hbar\delta\dot{\rho}_1 &= -\frac{\hbar^2\bar{\rho}_1}{m}\partial_x^2\delta\phi_1 - \hbar J\sqrt{\bar{\rho}_1\bar{\rho}_2}\sin\bar{\phi}\,(\delta_1+\delta_2) - 2\hbar J\sqrt{\bar{\rho}_1\bar{\rho}_2}\cos\bar{\phi}\,(\delta\phi_2-\delta\phi_1), \\ \hbar\delta\dot{\rho}_2 &= -\frac{\hbar^2\bar{\rho}_2}{m}\partial_x^2\delta\phi_2 + \hbar J\sqrt{\bar{\rho}_1\bar{\rho}_2}\sin\bar{\phi}\,(\delta_1+\delta_2) + 2\hbar J\sqrt{\bar{\rho}_1\bar{\rho}_2}\cos\bar{\phi}\,(\delta\phi_2-\delta\phi_1), \\ \hbar\delta\dot{\phi}_1 &= \frac{\hbar^2}{4m\bar{\rho}_1}\partial_x^2\delta\rho_1 - g\delta\rho_1 + \hbar J\sqrt{\frac{\bar{\rho}_2}{\bar{\rho}_1}}\left(\cos\bar{\phi}\,\frac{(\delta_2-\delta_1)}{2} - \sin\bar{\phi}\,(\delta\phi_2-\delta\phi_1)\right), \\ \hbar\delta\dot{\phi}_2 &= \frac{\hbar^2}{4m\bar{\rho}_2}\partial_x^2\delta\rho_2 - g\delta\rho_2 - \hbar J\sqrt{\frac{\bar{\rho}_1}{\bar{\rho}_2}}\left(\cos\bar{\phi}\,\frac{(\delta_2-\delta_1)}{2} + \sin\bar{\phi}\,(\delta\phi_2-\delta\phi_1)\right), \end{aligned} \tag{12}$$

where we define $\delta_j = \delta\rho_j/\bar{\rho}_j$. These equations are valid for linear perturbations around any arbitrary time-dependent homogeneous background. From now on, we focus on the π-state, which is characterized by closed classical trajectories in (ϕ, z) space around one of the non-equilibrium points, see Eq. (8). In this state, both the imbalance and the relative phase oscillate around a non-zero value. For more details on the dynamical regimes and the conditions for the π trapping, we refer to the discussion in Appendix A.1.

3.2 Tachyonic instability

We specify the linearized equations [Eq. (12)] to the π-trapped case by setting the fields to their stationary values [Eq. (8)]

$$\bar{\rho}_j \to \rho_j^*, \quad \bar{\phi} \to \pi, \tag{13}$$

and we choose, without loss of generality, that $\rho_1^* > \rho_2^*$.

For the analysis, it is convenient to introduce rescaled time τ and space $\tilde{x}$ as

$$\tau \equiv \frac{\mu}{\hbar}t, \quad \tilde{x} \equiv \frac{1}{\xi}x, \tag{14}$$

where the healing length ξ is defined as

$$\xi = \frac{\hbar}{\sqrt{m\mu}}. \tag{15}$$

Note that, therefore, frequencies are in units of $\mu/\hbar$ and hence have the same dimension as energies. Note that in the interest of readability, we omit the tilde when there is no risk of

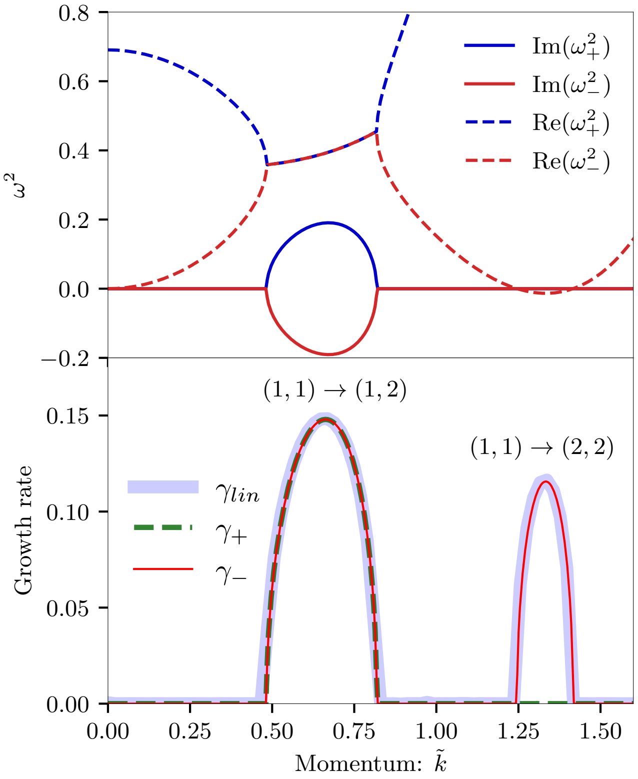

Figure 4: *Top:* Squared dispersion relation $\omega_\pm^2$ [Eq. (17)] as a function of momentum $\tilde{k}$ for $\Lambda = 3.55$. The real parts $\mathrm{Re}(\omega_\pm^2)$ and imaginary parts $\mathrm{Im}(\omega_\pm^2)$ of the squared dispersion relation $\omega_\pm^2$ are represented by solid and dashed lines, respectively. *Bottom:* Growth rates γ_+ (dashed line) and γ_- (thin solid line) corresponding to the imaginary part of ω_+ and ω_-, respectively [from Eq. (17)]. The growth rate γ_{lin} (thick solid line) is obtained from solving Eq. (12).

confusion. In terms of the rescaled variables, Eq. (12) reads in momentum space

$$
\begin{aligned}
\delta\dot{\rho}_1 &= \rho_1^* \tilde{k}^2 \delta\phi_1 + \frac{2}{\Lambda}\sqrt{\rho_1^*\rho_2^*}(\delta\phi_2 - \delta\phi_1),\\
\delta\dot{\rho}_2 &= \rho_2^* \tilde{k}^2 \delta\phi_2 - \frac{2}{\Lambda}\sqrt{\rho_1^*\rho_2^*}(\delta\phi_2 - \delta\phi_1),\\
\delta\dot{\phi}_1 &= -\left(\frac{\tilde{k}^2}{4\rho_1^*} + 1\right)\delta\rho_1 - \sqrt{\frac{\rho_2^*}{\rho_1^*}}\frac{(\delta_2 - \delta_1)}{2\Lambda},\\
\delta\dot{\phi}_2 &= -\left(\frac{\tilde{k}^2}{4\rho_2^*} + 1\right)\delta\rho_2 + \sqrt{\frac{\rho_1^*}{\rho_2^*}}\frac{(\delta_2 - \delta_1)}{2\Lambda},
\end{aligned}
\tag{16}
$$

where now the dot refers to the derivative with respect to τ. One observes from Eq. (16) that the dynamics of $\delta\rho_1, \delta\rho_2, \delta\phi_1$ and $\delta\phi_2$ is coupled to each other. Assuming the solutions have a time dependence $\sim \mathrm{e}^{-i\omega(\tilde{k})\tau}$, we find by diagonalization two pairs of eigenfrequencies $\omega_\pm(\tilde{k})$. Their squared dispersion relations are given by

$$
\omega_\pm^2(\tilde{k}) = \frac{X(\tilde{k})}{4\rho_{12}} \pm \frac{\sqrt{\Delta(\tilde{k})}}{2\rho_{12}^2},
\tag{17}
$$

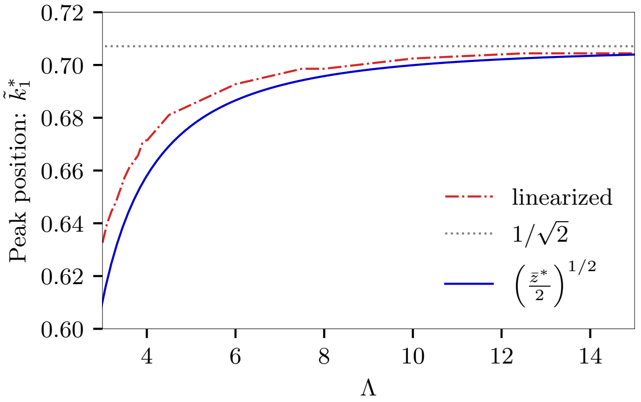

Figure 5: Prediction of the primary peak location at momentum $\tilde{k}_1^*$ versus the dimensionless ratio Λ. The analytical [Eq. (22)], numerical, and asymptotic results are indicated by a solid, dashed-dotted, and a dotted line, respectively.

where

$$X(k) = 2\Lambda^{-2} - 2\Lambda^{-1}\sqrt{\rho_{12}}\left(4\rho_{12} + k^2\right) + \rho_{12}k^2(2+k^2), \tag{18}$$

$$\begin{aligned}\Delta(k) =& \Lambda^{-2}\left[-4(\rho_{12})^{3/2} + \Lambda^{-1}\right]^2 - 2\Lambda^{-2}\sqrt{\rho_{12}}\left[\Lambda^{-2} + \sqrt{\rho_{12}}\left((\rho_1^*)^2 - 6\rho_{12} + (\rho_2^*)^2\right)\right]k^2 \\ &+ \rho_{12}\left[2\Lambda^{-1}\sqrt{\rho_{12}}(\Delta\rho)^2 + \rho_{12}(\Delta\rho)^2 + \Lambda^{-2}\right]k^4,\end{aligned} \tag{19}$$

and, for brevity, $\rho_{12} = \rho_1^*\rho_2^*$ and $\Delta\rho = \rho_1 - \rho_2$. The squared eigenvalues $\omega_\pm^2$ are shown in the top plot of Fig. 4 as a function of scaled momentum. The real parts $\mathrm{Re}(\omega_\pm^2)$ and imaginary parts $\mathrm{Im}(\omega_\pm^2)$ are indicated by dashed and solid lines, respectively. From this, one can conclude that the system becomes unstable in two sets of momentum modes for different reasons. The population of these sets of unstable momentum modes grows exponentially. In fact, there is a first range of modes that experience a positive growth rate because $\mathrm{Re}(\omega_-^2) < 0$. This kind of instability is commonly referred to as *tachyonic* instability in a cosmological context [44]. The second region of dynamical instability in the system arises when, in the squared dispersion relation, the square root argument $\Delta(k) < 0$. We note that there are no additional primary unstable regions in the system.

The growth rates γ_+ and γ_-, associated with the analytical prediction for the imaginary part of the eigenvalues ω_+ and ω_-, are shown in the bottom plot of Fig. 4 by the dashed and thin solid lines, respectively. The γ_{lin} represents the growth rate computed numerically by solving the linearized equations of motion [Eq. (12)], and the thick solid line indicates it. The analytical results match the numerically computed growth rates derived by the full solution of the system of linearized equations.

3.2.1 Physical interpretation

The physical process underlying this instability consists of the excitation of a pair of particles from the first condensate. This can happen when one or both particles tunnel to the second condensate, leading to an energy excess that gives them momentum. Note that in 0D, this is not possible due to energy *and* momentum conservation. By symmetry, this decay occurs as the emission of atom pairs in opposite directions, i.e., twin beams with momentum $\pm\tilde{k}^*$. The pairs are produced with equal and opposite wavenumber $\pm\tilde{k}^*$ in each wire, a process that we will refer to $(1,1) \to (l,m)$ for two particles starting from the first condensate and produced in the wells l and m, where $l,m = 1,2$. Note, that in contrast to the twin beam experiment [45], no further selection rules apply here, such that all processes that conserve energy are allowed.

A simple perturbative calculation treating the tunneling term as a perturbation can help gain physical insight. First, let us examine more in detail the $(1,1) \rightarrow (1,2)$ process, shown in Fig. 6*a*). The dominant contribution to particle creation comes from the momentum mode satisfying the resonant condition

$$\epsilon_1(\tilde{k}) + \epsilon_2(\tilde{k}) = \frac{\Delta\mu}{\mu}, \tag{20}$$

which equals the sum of energies of the particles each excited in one well, given by the Bogoliubov dispersion relation for the case of a free condensate

$$\epsilon_j(\tilde{k}) = \sqrt{\tilde{k}^2\left(\frac{\mu_j}{\mu} + \frac{\tilde{k}^2}{4}\right)}, \tag{21}$$

to the scaled difference of chemical potentials $\Delta\mu/\mu = (\mu_1 - \mu_2)/(\mu_1 + \mu_2)$. The solution of Eq. (20) gives the resonant momentum

$$\tilde{k}_1^* = \left(\frac{\bar{z}_0^*}{2}\right)^{1/2} = \left(\frac{1}{4} - \frac{1}{\Lambda}\right)^{1/4}, \tag{22}$$

that corresponds to the center of the first instability peak in the bottom plot in Fig. 4. Therefore, the specific location of the peak only depends on the specific choice of the dimensionless parameter Λ. A comparison between the analytical and numerical results can be seen in Fig. 5. The analytical prediction [Eq. (22)], shown with dashed lines and detailed in Ref. [30], is compared to the numerical result obtained by solving the linearized equation and fitting the growth rate, shown with a solid line. The deviation from the analytical, theoretical prediction is due to numerical uncertainty and the approximation to a weakly tunnel-coupled system. Asymptotically, for $\Lambda \gg 1$, $\tilde{k}_1^* \rightarrow 1/\sqrt{2}$, indicated as a dotted horizontal line in the figure.

The second process which is energetically allowed is $(1,1) \rightarrow (2,2)$, shown in Fig. 6*b*). Energy conservation gives the resonant condition

$$2\epsilon_2(\tilde{k}) = 2\frac{\Delta\mu}{\mu}. \tag{23}$$

Proceeding in a similar fashion as in the previous case, the solution of Eq. (20) gives the resonant momentum $\tilde{k}_2^*$ that corresponds to the center of the second instability peak in Fig. 4.

In both cases, we obtain the same results for the peak location for the instability as discussed in Ref. [33] for the limiting case of large Λ, even though the reference studies the different dynamical regime of MQST. In fact, the actual physical process of pair creation and redistribution in the wells is identical to our case.

3.3 Linearization for oscillating mean fields: parametric instabilities

After discussing the linearization around the stationary point in (ϕ, z) space, we now want to generalize this approach to generic (time-dependent) closed trajectories around it. In this case, there is an additional instability, parametric resonance, caused by the oscillatory behavior of the mean fields. The oscillations around the minimum of the effective potential act as a source for a parametric resonance instability, in addition to the tachyonic instability discussed before. In fact, an entire range of modes experiences a positive growth rate, and the width of this instability band increases with the modulation amplitude $\Delta z = z_0 - z_0^*$. First, we get a qualitative understanding of the mechanisms behind the additional peaks.

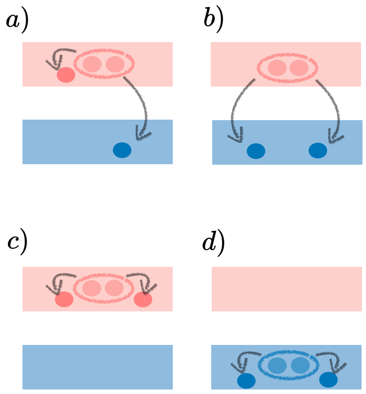

Figure 6: Physical processes related to the primary instability of the coupled BEC system with components Ψ_1 and Ψ_2, indicated by the upper and lower elongated shapes, respectively: a) excitation of a pair of particles from the first condensate, where one particle further tunnels to the second condensate; b): excitation of a pair from the first condensate that tunnels to the second one; c) and d): excitation of a pair of particles from each of the two condensates.

3.3.1 Physical interpretation

Once again, we can use energy arguments, as explained below, to gain an intuitive understanding of the underlying physical processes that lead to the different peaks. We will treat the condensate as very weakly coupled to use the free dispersion relation. This procedure is justified because the ratio $1/\Lambda$ is small. In the following, we explain the origins from resonance conditions. As in the previous subsection, we will indicate the process where two particles from condensate j are excited, and end up in the l and m wells as $(j,j)\xrightarrow{r}(l,m)$, where the 'r' is indicating that the mechanism behind the excitation of the pair is parametric resonance. The allowed processes are the following:

- $(j,j)\xrightarrow{r}(j,j)$
  These two cases correspond to a pair of particles leaving a condensate in a given well $j=1,2$, which gets excited by higher momentum modes in the same well. The resonance occurs when the Bogoliubov dispersion relations [Eq. (21)] match the frequency ω_r of the oscillation frequency of the imbalance densities $\bar{\rho}_j$ (which equals the oscillation frequency of the trapped relative phase $\bar{\phi}$ since they are conjugate variables). In this case, energy conservation yields

  $$2\epsilon_j=\omega_r. \tag{24}$$

  The same result for the location of the unstable modes can also be estimated in a different way, which connects with the usual discussion of parametric resonance in field theory. Specifically, for small oscillation amplitudes (i.e., when $\Delta z \ll 1$), by taking a further time derivative of the density equations in Eq. (16) and taking the limit of uncoupled condensates, and slowly varying mean fields, the resulting equations can be brought to the form of a Mathieu equation [46, 47] in terms of the $\delta\rho_j$ alone,

  $$\left[\frac{\partial^2}{\partial s^2}+A_{\tilde{k}}-2q_{\tilde{k}}\cos(2s)\right]\delta\rho_j(s,\tilde{k})=0, \tag{25}$$

  with the dimensionless time $s=\omega_r\tau/2$, and parameters $A_{\tilde{k}}=\epsilon_j^2(\tilde{k})/(\omega_r/2)^2$ and $q_{\tilde{k}}=\Delta z\epsilon_{\tilde{k},0}\mu_j/(\omega_r/2)^2$. Equation (25) admits oscillatory solutions with exponentially

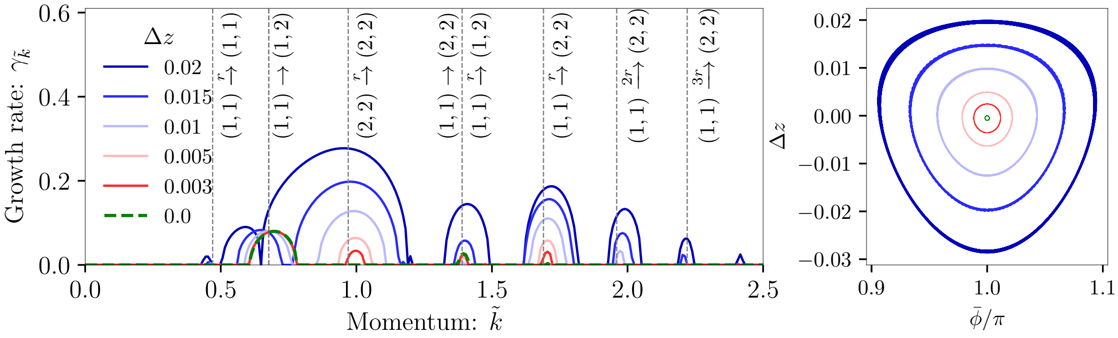

Figure 7: Instability chart as a function of the wavenumber $\tilde{k}$ for the *oscillating* π-mode with varying initial conditions Δz. The oscillations and amplitude of the mean fields are shown in the inset and legend, respectively. We choose $\Lambda = 7.10$ for better comparison with the analytical predictions for the location of the peaks, see the main text for details. The vertical dashed lines indicate the position of the maximum of the instability band from the analytical calculation. The tachyonic instabilities $(1,1) \to (1,2)$ and $(1,1) \to (2,2)$ are indicated with dashed lines. Parametric instabilities from left to right: leading resonance $(1,1) \xrightarrow{r} (1,1)$ and leading resonance $(2,2) \xrightarrow{r} (2,2)$ [Eq. (24)], resonance $(1,1) \xrightarrow{r} (1,2)$ [Eq. (28)], leading resonance $(1,1) \xrightarrow{r} (2,2)$ [Eq. (27)], second order resonance $(1,1) \xrightarrow{2r} (2,2)$, third order resonance $(1,1) \xrightarrow{3r} (2,2)$.

growing amplitudes that describe parametric resonance. The width of this instability band is delimited by the modes satisfying

$$A_{\tilde{k}} = 1 \pm q_{\tilde{k}}, \tag{26}$$

which increases with the amplitude r of the oscillation. That is, resonance occurs for those momentum modes whose energy equals half a quantum of energy $\hbar\omega_r/2$ injected in the system through the oscillation at frequency ω_r.

- $(1,1) \xrightarrow{r} (2,2)$
  It can also occur that from the first condensate, a pair of atoms get excited to the second condensate. In Fig. 6, c) and d) represent the physical process of two particles leaving the condensate end and getting excited at opposite momenta from

$$2(\epsilon_2 - \frac{\Delta\mu}{\mu}) = \omega_r. \tag{27}$$

- $(1,1) \xrightarrow{r} (1,2)$
  The last case occurs when a pair of particles from the first condensate gets excited by the driving force of the oscillations, and only one atom tunnels to the other condensate. In this case,

$$\epsilon_1 + \epsilon_2 = \omega_r + \frac{\Delta\mu}{\mu}. \tag{28}$$

  The resonance peak overlaps with the tachyonic peak discussed in the previous subsection. Still, we see that for increasing oscillation amplitude, the corresponding growth rate first appears even without oscillations being present ($\Delta z = 0$), then diminishes and then takes over growing in amplitude.

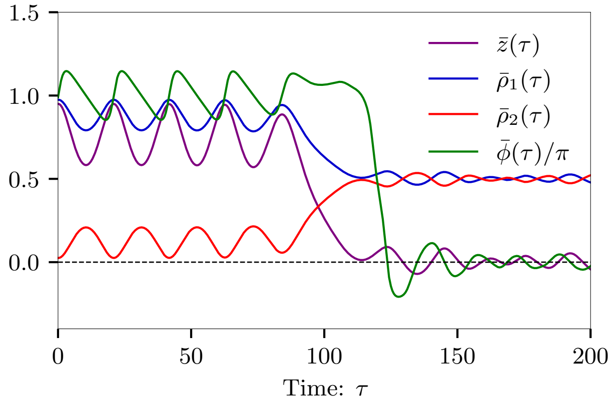

Figure 8: Time evolution of the densities in the two condensates $\bar{\rho}_j(\tau)$, relative imbalance $\bar{z}(\tau)$ and relative phase $\bar{\phi}(\tau)$. The π-trapped state was initialized in $(z_0, \phi_0) = (0.95, \pi)$ with $\Lambda = 3.55$. The oscillations of the fields are followed by the equilibration of the imbalance and relative phase to zero at late times (dashed line).

Moreover, for each resonance process, the above analysis only concerned the first (order) instability band. Still, in general, multiples of the resonance, so higher frequency harmonics are also in resonance. Each band in momentum space has a width of order $\delta\tilde{k} = l^2$, $l \in \mathbb{N}$. So they will be located at higher frequencies (but not multiples), with a narrower width, and a lower growth rate. We denote these processes in the figure as $(i,j) \xrightarrow{lr} (i,j)$ to indicate the l-order resonance.

In general, for increasing the oscillation amplitude Δz, the width of the parametric instability bands increases and the bands higher. There are no further resonance processes apart from the ones discussed. For instance, the process involving a pair of particles from the second condensate with one (or more) particles tunneling to the second condensate is energetically forbidden. The instability chart is summarized in the left panel of Fig. 7, along with the evolution of the mean fields displayed in the right panel. Energetically possible processes are represented by vertical lines. The dashed green line illustrates the limiting case where only tachyonic instabilities are present, occurring when the amplitude of the mean fields' oscillation approaches zero.

4 Beyond linearization with numerical simulations

The previous section gave a linearized analysis of the evolution of perturbations, allowing us to gain an analytic understanding of the primary instabilities. In this section, we solve the full GPE equations with initial fluctuations as a seed for the instabilities. We refer to Appendix B for a review of the method and the implementation details. In order to observe the instabilities more clearly, we first reduce the noise to $\eta = 0.001$ (see Eq. (B.1) for the definition of the noise factor η). Later in Sec. 4.1.4, we will examine the case of vacuum and thermal noise.

For all simulations, we have considered typical values for an experiment using ^{87}Rb: $m = 87$ amu, $a_s \approx 5.2$ nm, the longitudinal trapping potential $\omega_\perp = 2\pi\nu_\perp$, $\nu_\perp = 1.4$ kHz. We consider a homogeneous system ($\omega_\parallel = 0$). The tunneling coupling $J = 2\pi\nu_J$, has been set to $\nu_J = 200$ Hz. Furthermore, we consider 20000 particles and 2048 lattice points with equal spacing $a = 0.1$ μm, corresponding to typical experimental densities $\rho \approx 100$ atoms per μm. In our classical-statistical simulations, we typically average over at least 200 runs.

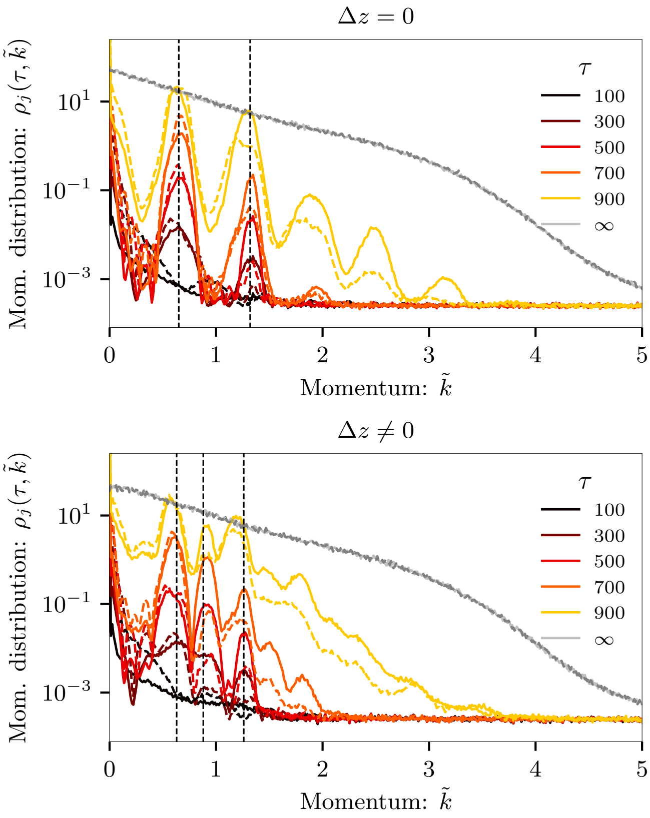

Figure 9: Momentum distribution of the condensates (solid and dashed lines correspond to the first and second condensate, respectively) for the π-trapped state at different times. The black dashed lines show the maximally unstable momentum modes obtained using energy considerations (see Sec. 3.2.1). *Upper:* Fields initialized in the mean field stationary point $(\phi_0, z_0) \approx (\pi, z_0^*)$. *Lower:* Fields initialized in $(\phi_0, z_0) = (\pi, 0.95)$, corresponding to weak oscillations around the mean-field stationary points, i.e., $\Delta z \neq 0$. These initial conditions cause the same instabilities as the $\Delta z = 0$ case, but additional peaks arise due to oscillations in phase and imbalance that cause parametric resonance.

As in the previous section, we first present results for initial conditions for the fields at the saddle point and then generalize to small oscillations around it. These numerical simulations enable us to study also the non-linear dynamics: In Fig. 8, the time evolution of the fractional imbalance z and relative phase ϕ is shown. At late times, the system deviates from the classical trapped trajectory, showing damping [48] and eventually approaching equilibrium where both the relative phase and the imbalance vanish. As z and ϕ are canonically conjugate variables, density fluctuations reach their maximum when phase fluctuations cross zero and vice versa.

The relevant observable for the study of the growth of fluctuations is the momentum distribution

$$\rho_j(\tau, \tilde{k}) = \frac{1}{L} \overline{\Psi_j(\tau, \tilde{k}) \Psi_j^*(\tau, \tilde{k})}, \tag{29}$$

where $\Psi_j(\tau, \tilde{k}) = \int \mathrm{d}\tilde{x} \Psi_j(\tau, \tilde{x}) \mathrm{e}^{-i\tilde{k}\tilde{x}}$ denotes the Fourier transform of the field and the notation $\overline{(\ldots)}$ refers to the ensemble average across all realizations. The momentum distribution is shown in Fig. 9 for the two cases with identical parameters as examined earlier.

The simulations show the primary instabilities at early times already discussed using the Bogoliubov approximation in Sec. 3. As the occupation number of unstable modes increases

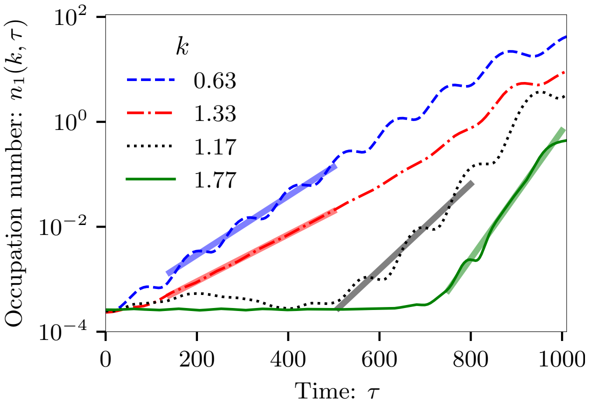

Figure 10: Time evolution of the occupation number of primary and secondary exponentially unstable modes in the first wire, The dashed and dotted-solid lines correspond to the two maximally unstable modes, also shown in Fig. 9. The straight lines indicate the corresponding growth rate $\gamma_{j,lin}$ as predicted by the linearized theory. The black-dotted and green solid curves are the secondary unstable modes with enhanced growth rates.

exponentially, they become highly occupied, and the system enters a non-linear regime. The Bogoliubov approximation breaks down, and the stage of secondary amplification sets in. As time progresses, the system deviates from the linear regime, which we discuss next. Our analysis follows a similar approach as in Ref. [35].

The emergence of both primary as well as secondary instabilities can be observed from the results of the numerical lattice simulations shown in Fig. 9. The black dashed lines show the predicted peaks according to energy conservation (as already discussed in Sec. 3.3.1). The peaks correspond to the maximally unstable modes of the linearized theory within each instability band (cf. Fig. 7).

Figure 10 shows the time evolution of the most unstable modes corresponding to the primary and secondary peaks in the first wire. The dotted blue and dashed-dotted red curves represent the primary unstable modes, while the black dotted and green solid curves correspond to the secondary unstable modes with enhanced growth rates. As it can be observed, the secondary modes begin to grow later, around $\tau \approx 600-800$, but then grow at a faster rate than the primaries. The straight lines represent exponential growth with a corresponding growth rate $\gamma_{j,lin}$, where $j = 1,2$ indicates the prediction by the linearized theory, corresponding to momenta $\tilde{k}_j^*$. It's worth noting that the result from the linearized theory is slightly higher than the GPE, but the presence of noise can account for this difference.

When macroscopically occupied modes start interacting, the mode with momentum $3\tilde{k}^*$ starts growing due to the dominant scattering process $(\tilde{k}^*, \tilde{k}^*) \rightarrow (-\tilde{k}^*, 3\tilde{k}^*)$ [35]. Furthermore, the momentum modes at $\pm\tilde{k}^*$ can also engage in interactions with the condensate mode of Ψ_1. This process is expected to increase the occupation number of the $2\tilde{k}^*$ mode [35].

Over time, the process of the secondary instabilities continues, resulting in the occupation of progressively higher modes. An alternative approach to study these secondary instabilities is, rather than letting the time evolution fill these excited modes, to directly seed the primary modes, as discussed in Ref. [35]. At later times, the growth of all modes deviates from the exponential growth and then eventually stops, as no single process dominates the dynamics. In this final phase, the distinct peak structure of the spectrum is lost, particles spread across various momentum modes, and the system undergoes thermalization (represented by gray lines for $\tau \rightarrow \infty$ in Fig. 9).

4.1 Experimental feasibility and finite temperature

In this section, we outline the requirements for experimentally investigating the π-state dynamics studied in this work. For a quantitative comparison with realistic experimental parameters, we refer to Fig. 3 and Eqs. (9) and (10). These define the necessary conditions $\Lambda \in (\Lambda_b, \Lambda_u)$ for the appearance of the π-oscillations in the dimensionless (Λ, z_0) space. In general, its stability is determined by the appearance of non-trivial scattering solutions related to the emission of correlated pairs of excitations, as explained in Sec. 3. Therefore, by increasing the system size L along the extended direction of the bosonic Josephson junction, the system transitions from stable π-oscillations, as predicted by the two-mode (mean-field) model, to the reported instabilities. The specific parameter regimes we considered in the previous sections are readily implementable in present-day experiments with quasi-1D Bose gases [30]. However, our analysis so far has been based on a more idealized scenario than actual experiments. In the following, we will explain and justify the approximation to the homogeneous quasi 1D model Eq. (1), discuss the preparation of the π-state and the experimental measurement procedure, and lastly, show the persistence of the predicted dynamics at finite temperature.

4.1.1 Validity of the 1D model

The validity of the one-dimensional model Eq. (1) [49–51], as well as its low energy effective description in terms of the sine-Gordon model [52], have been shown in previous Atomchip experiments. In particular, this has been shown for Josephson oscillations [17, 32], Floquet engineered bosonic Josephson junctions [53], and the effective low-energy description for balanced condensates [14, 54, 55].

Here, we briefly discuss two relevant details related to atom trapping in an external potential. In fact, in any experiment, atoms are confined in an external potential. Digital micromirror devices (DMDs) enable precise control over the shape of the trapping potential [56,57]. Homogeneous box traps, for which the density inhomogeneities are concentrated close to the boundaries, are nowadays readily available in cold-atom experiments. In contrast to, e.g., harmonic trapping, the dynamics within the bulk is therefore well approximated by a homogeneous system (see e.g. [58]). More precisely, as long as the timescales of the instability dynamics is short compared to the propagation speed of fluctuations originating from the boundary, the influence of the potential can be neglected.

Moreover, the one-dimensional approximation we considered neglects interaction-induced broadening of the wavefunction in the radial directions [51,59]. A more precise derivation of the one-dimensional model would, therefore, in general, include non-trivial density dependencies of the coupling constants (see e.g. [58]). While strictly the system becomes non-integrable and described by the non-polynomial Schrödinger equation [59], its dominant mean-field effect on the dynamics of the linearized fluctuations is a small renormalization of the tunnel-coupling J and the speed of sound c_s. While the former only needs to be considered when determining the correct parameter regime (i.e., the dimensionless Λ), the latter simply leads to a trivial shift of the resonances (in SI units).

4.1.2 State preparation

A detailed analysis of the dynamical preparation process goes beyond the scope of this paper. Here, we give an overview of established techniques for future experimental implementation of the π-state. Atomchips [60–62] enable precise creation and control of a double-well (DW) potential for 1d quantum gases on timescales much faster than the typical timescale of the reported instabilities [63–65]. In particular, this includes: (i) variation of the tunneling coupling

J (see e.g. [14]), (ii) tilting or rotation of the DW potential [63], and (iii) Floquet engineering [53].

The precise control of the DW potential facilitates a number of prospective preparation sequences, even for the stationary DW system. Reaching the correct dimensionless parameters is a matter of optimization, as procedures (i) and (ii), in principle, permit independent control of the state in the (Λ, z_0) space. More critical for observing the π-state dynamics, as opposed to MQST, is the preparation of the initial relative phase difference.

Coherent splitting ($J \to 0$) of a thermal state of a single condensate or a strongly tunnel-coupled DW preserves the initial relative phase between the two condensates close to zero, while an additional tilt of the DW potential can be used to tune the mean-field imbalance z_0. The simplest approach reaching the π-state, relies on direct control of the individual potentials for each well (or at least the gradient between them). In this case, using a DMD, the initial relative phase can be adjusted through direct phase imprinting.

Another possibility is based on exact timings such as, e.g. accumulation of a global relative phase over time, due to the density imbalance and/or additional tilting of the DW. Note that this phase accumulation can be tuned to timescales much faster than the longitudinal dynamics. Lastly, rapidly recombining the condensates to finite coupling J starts the dynamics and decay of the π-state reported here. Optimal control methods for the considered system (see e.g. [66–68]) can be used to further minimize unwanted disturbances of the preparation process, such as e.g. radial sloshing, or to lower the initial relative temperature after the splitting process via optimal-control [66, 67].

For the Floquet engineered bosonic Josephson junction the initial relative phase difference between the two condensates can be adjusted by choosing the phase of the Floquet driving. Varying its magnitude changes the Floquet assisted effective tunneling rate, and hence the relevant parameter Λ. While preparation of the π-state is comparatively simple in this system, Floquet driving will inevitably increase the amount of noise present in the system.

4.1.3 Relevant observables and their measurement

The simplest indicator of the decay of the π-state is the time evolution of the mean-fields $\bar{z}(t)$ and $\bar{\phi}(t)$, as presented in Fig. 8. However, the primary observable for investigating specifics of the decay is the momentum distribution of excitations within each well.

In cold-atom experiments, the time evolution of these observables is commonly measured via destructive measurement. A measurement cycle consists of:

(i) Initializing the π-state,

(ii) Holding it within the trap for a fixed time t during which the unitary dynamics takes place,

(iii) Releasing the atoms by switching off all external trapping potentials,

(iv) Letting the system evolve freely for an additional time-of-flight t_{ToF}, and

(v) Imaging the atomic density and extracting the relevant observables.

Quantum mechanical averages of correlations are obtained by averaging the experimental results over many independent realizations. In step (iii), the two clouds can either be simply released from the trap and let interfere or given an additional kick (momentum) in the double-well direction to separate particles in the left and right well during the time-of-flight dynamics.

For an intermediate time-of-flight $t_{\mathrm{ToF}} \lesssim 15\,\mathrm{ms}$, the former procedure gives direct access to the spatially-resolved relative phase between the two condensates through matter-wave interference [69]. The spatially resolved relative density fluctuations are, in principle, accessible

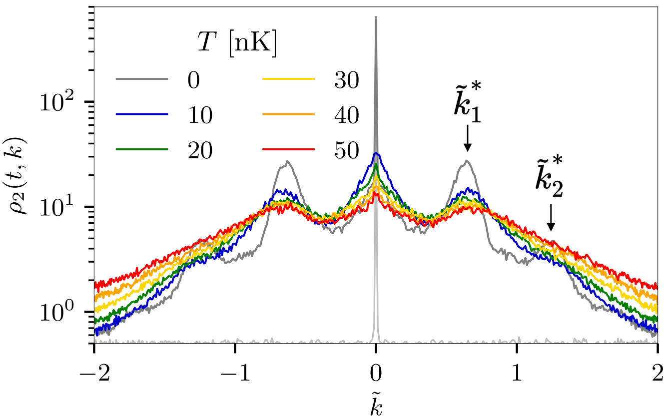

Figure 11: Momentum distribution in the second well ρ_2 for temperature $T = \{0, 10, 20, 30, 40, 50\}$ nK at $t = 3.8$ ms (this timescale corresponds in dimensionless units to $\tau \approx 300$ in Fig. 9).

through full tomography of the relative degree of freedom [70]. The latter procedure allows us to measure the density imbalance directly, as the two clouds do not interfere. Recent results combining the two techniques through partial out-coupling of atoms demonstrated simultaneous measurement of both quadratures [71], i.e. the Husimi-distribution of the non-commuting relative density and phase variables.

Further, the individual momentum distributions of the atoms in the left and right well can be measured after a long time-of-flight $t_{\mathrm{ToF}} \approx 46\,\mathrm{ms}$ in a light-sheet with single-atom sensitivity [17, 72]. Note that due to the rapid expansion in the tightly confined radial directions, the time-of-flight evolution is for $t_{\mathrm{ToF}} \gtrsim 1\,\mathrm{ms}$ well approximated by the non-interacting Schrödinger equation and hence conserves the momentum distribution along the extended direction. Additionally, the effective imaging resolution of the experiment can be further enhanced in real space in the ultraviolet momentum scales through the magnification of the in-situ cloud via magnification of the density distribution via matter wave optics (cf. [73]) or in momentum-space in the infrared momentum scales through condensate focusing [74], which shifts the respective plane of focus to a variable finite time t_{ToF}.

Spatially resolved interference along the extended direction allows the extraction of the occupation of the linearized fluctuations, while the momentum distribution of the atoms is directly measured for long t_{ToF}. Note that linearized fluctuations rapidly coincide with single-atom excitations for $\tilde{k} > 1$ i.e. within the dispersive branch of the linearized Bogoliubov dispersion relation. The average momentum distribution $\rho_{1,2}(t, \tilde{k})$ can be directly compared to the predictions of the linearized theory.

4.1.4 Finite Temperature

One of the major experimental limitations for observing the presented dynamics is the amount of noise in the system. At the beginning of this section, we considered a reduced noise level to make the different stages of the evolution visible. For increasing noise, this clear separation into periods of linear primaries, a limited number of non-linear secondaries, and a late stage of complete non-linear thermalization disappears. This, in general, presents one of the major challenges in experimentally observing secondaries in analog field theory simulations, with a recent measurement for classical water-air interfacial waves [75].

We display in Fig. 11 the momentum distribution of the empty well ρ_2 at $t = 3.8\,\mathrm{ms}$ for different initial temperatures $T = 0 - 50\,\mathrm{nK}$. The empty well was initialized by sampling the quantum noise within the quasiparticle particle basis (see Appendix B for more details on the numerical implementation). Around this timescale, the primary instability peaks are clearly visible at $T = 0$, with the two momentum peaks located at $\tilde{k}_1^*$ and $\tilde{k}_2^*$. The primary instability peak located at $\tilde{k}_1^*$ remains visible and in good agreement with theoretical predictions for temperatures easily achievable with current cold-atom experiments. Note that for even higher temperatures, we find a slight shift of the instability peaks to higher momenta.

Detecting the relevant higher-loop processes experimentally could be difficult at higher temperatures. To overcome this limitation, one approach is to seed the primary instabilities, as done, e.g., in Ref. [35], and/or further decrease the temperature [76, 77]. Further, the decay processes are expected to create excitations in pairs, leading to higher-order correlations between different momentum modes, similar to the studies performed in Refs. [45, 78]. A detailed analysis of the pair-correlations and their decoherence due to finite temperature is beyond the scope of this paper.

5 Conclusions

In this work, we investigated the dynamics of two weakly tunnel-coupled quasi-one-dimensional Bose gases in the π-state. While the system exhibits π-oscillations classically under the condition that the ratio of the chemical potential to the tunneling energy is sufficiently large and the initial energy above a critical value, this state becomes unstable due to quantum fluctuations.

We studied the early time dynamics by linearizing the theory and observed that the state deviates from the mean-field prediction. At first, we examined the simpler case of the system initialized such that the oscillations are suppressed, and the fields remain constant, identifying tachyonic instabilities. Secondly, we also generalized our analysis to oscillating fields, producing additional parametric resonance instabilities. Physically, the instability is due to the excitation of quasiparticle pairs from the two condensates to characteristic bands of momenta. The occupation of these modes grows exponentially, and the momentum peaks can be predicted analytically using energy considerations. We analyzed in detail the different mechanisms underlying the pair production.

Later in the dynamics, the system develops a very sharp momentum distribution, where the linear theory breaks down. We go beyond linearization by means of GPE numerical simulations, in particular, to study the formation of secondary instabilities. Eventually, at late times, the system generally reaches a steady state, at which point the momentum distributions in the two wires become the same, and the relative phase vanishes.

Our analysis provides detailed results on the instability dynamics and decay of the π-mode. This provides an important prerequisite for possible experimental realizations in a BEC system. To this end, we also studied finite temperature initial conditions for which we find that the primary instabilities remain observable within the typical range of parameters accessible in current experiments.

Acknowledgements

We thank Stefan Floerchinger, Michael Heinrich, Eduardo Grossi, Louis Jussios, Silke Weinfurtner, and Tiantian Zhang for valuable discussions.

Funding information L.B., S.E., J.S., and J.B. acknowledge support by the DFG / FWF under the Collaborative Research Center SFB 1225 ISOQUANT (Project-ID 27381115, Austrian Science Fund (FWF) I 4863). S.E. acknowledges additional support by the Austrian Science

Fund (FWF) [Grant No. I6276, QuFT-Lab].

A Mean-field approximation

This appendix contains the derivation on the mean field equations [Eq. (6)].

A.1 Equations of motion

The classical equations of motion correspond to the zeroth order in a perturbative expansion of the full GPE [Eq. (3)] in terms of fluctuations. The equation for the Ψ_j field becomes, in the phase-density representation [Eq. (4)]

$$\frac{i\hbar\dot{\bar{\rho}}_j}{2\sqrt{\bar{\rho}_j}}\mathrm{e}^{i\bar{\phi}_j}-\hbar\dot{\bar{\phi}}_j\sqrt{\bar{\rho}_j}\mathrm{e}^{i\bar{\phi}_j}=g\bar{\rho}_j\sqrt{\bar{\rho}_j}\mathrm{e}^{i\bar{\phi}_j}-\hbar J\sqrt{\bar{\rho}_l}\mathrm{e}^{i\bar{\phi}_l}, \tag{A.1}$$

with $j\neq l$. Multiplying both sides by $\sqrt{\bar{\rho}_j}$ leads to

$$\frac{i\hbar\dot{\bar{\rho}}_j}{2}-\hbar\bar{\rho}_j\dot{\bar{\phi}}_j=-\hbar J\sqrt{\bar{\rho}_j\bar{\rho}_l}[\cos(\bar{\phi}_l-\bar{\phi}_j)-i\sin(\bar{\phi}_l-\bar{\phi}_j)]+g\bar{\rho}_j^2. \tag{A.2}$$

Now, the equations of motion for the density and phase fields can be deduced by separating Eq. (A.2) into the imaginary and real parts, respectively, giving

$$\begin{aligned}\hbar\dot{\bar{\rho}}_j&=2J\hbar\sqrt{\bar{\rho}_j\bar{\rho}_l}\sin(\bar{\phi}_l-\bar{\phi}_j),\\ \hbar\dot{\bar{\phi}}_j&=\hbar J\sqrt{\frac{\bar{\rho}_l}{\bar{\rho}_j}}\cos(\bar{\phi}_l-\bar{\phi}_j)-g\bar{\rho}_j.\end{aligned} \tag{A.3}$$

Finally, the equations of motion can be expressed in terms of the relative degrees of freedom $\bar{z}$ and $\bar{\phi}$, leading to Eq. (6).

A.2 An effective motion in a quartic potential

The equations of motion for the background fields z,ϕ [according to Eq. (6), where we drop the bar and the explicit dependence on time here for the sake of notational simplicity] can be recast in an effective equation of motion for the fractional population imbalance moving in an effective potential $V(z)$ as the following. To reduce the number of variables to a single one, we can use that energy (from now on we set $\hbar=1$)

$$H=\frac{\mu z^2}{4}-J\sqrt{1-z^2}\cos\phi \tag{A.4}$$

is conserved, i.e.,

$$H=H_0\equiv H(t=0)=\frac{\mu z_0^2}{4}-J\sqrt{1-z_0^2}\cos(\phi_0). \tag{A.5}$$

As a result, the phase variable ϕ can be eliminated, and the resulting equation of motion for z is given by the following equation

$$\ddot{z}=\left(2\mu H_0-4J^2\right)z-\frac{\mu^2}{2}z^3\equiv-\frac{\partial V}{\partial z}. \tag{A.6}$$

In other words, the imbalance is effectively moving in a classical effective potential $V(z)$. The potential is obtained by integrating Eq. (A.6) and results in

$$V(z) = -\left(\mu H_0 - 2J^2\right)z^2 + \frac{\mu^2}{8}z^4. \tag{A.7}$$

The stationary point occurs when the initial condition z_0 aligns with the minimum of the effective potential, leading to Eq. (8).

In the case where the initial imbalance is very strong and $\Lambda \ll 1$, we have $H_0 \approx \mu/4$. In this scenario, Eq. (A.6) reduces to

$$\ddot{z} + \left(\frac{\mu^2}{2} - 4J^2\right)z - \frac{\mu^2}{2}z^3 = 0. \tag{A.8}$$

The exact solution can be expressed in terms of Jacobi elliptic functions [79]

$$z(\tau) = \mathrm{dn}\left(\frac{2\tau}{\mu}, \frac{\Lambda}{4}\right). \tag{A.9}$$

B Classical-statistical simulations

In this appendix, we summarize the main information about the implementation of the GPE numerical simulations presented in Sec. 4.

B.1 Numerical implementation

The numerical technique of classical-statistical simulations (also known as truncated Wigner simulations) incorporates quantum fluctuations through stochastic initial conditions, while the time evolution is deterministic and defined by classical equations of motion (see e.g. [80,81]). The observables consist of quantum expectation values obtained via statistical averages across a large number of independent realizations [38]. In this work, we examine homogeneous scalar BECs, either at zero or finite temperature, defined on a spatial grid of length L with periodic boundary conditions. For a single realization, we sample the initial field configuration from the Wigner distribution of the initial state, here taken to be the vacuum or thermal equilibrium state of the Bogoliubov quasiparticles, as

$$\Psi_j(0,x) = \sqrt{\rho_j(0)}\mathrm{e}^{i\phi_j(0)} + \sqrt{\frac{\eta}{2}}\sum_{k\neq 0}\left[\alpha_{k,j}u_{k,j}(x) - \alpha^*_{k,j}v^*_{k,j}(x)\right]. \tag{B.1}$$

The parameter η is used to control the level of noise, with $\eta < 1$ reducing the vacuum noise below the average occupancy of half a particle per mode, i.e., the "quantum one-half." Explicit expressions for $u_{k,j}(x)$ and $v_{k,j}(x)$ are given by $u_{k,j}(x) = u_{k,j}\mathrm{e}^{ikx/\hbar}/\sqrt{L}$ and $v_{k,j}(x) = v_{k,j}\mathrm{e}^{ikx/\hbar}/\sqrt{L}$, and

$$u_{k,j} = \sqrt{\frac{1}{2}\left(\frac{\xi_{k,j}}{\epsilon_{k,j}} + 1\right)}, \qquad v_{k,j} = \sqrt{\frac{1}{2}\left(\frac{\xi_{k,j}}{\epsilon_{k,j}} - 1\right)}, \tag{B.2}$$

are the solutions of the Bogoliubov-de-Gennes equations for a uniform system in a periodic box, with real coefficients $\epsilon_{k,j} = \sqrt{\epsilon_{k,0}(\epsilon_{k,0} + \rho_{0,j}g)}$, $\xi_{k,j} = \epsilon_{k,0} + \rho_{0,j}g$, and $\epsilon_{k,0} = (\hbar k)^2/(2m)$. It holds that $\left|u_{k,j}\right|^2 - \left|v_{k,j}\right|^2 = 1$. The quasiparticle amplitudes $\alpha_{k,j}$ in Eq. (B.2) are sampled as

$$\alpha_{k,j} = \sqrt{n_{BE,kj} + \frac{1}{2}}\frac{x_k + iy_k}{\sqrt{2}} \tag{B.3}$$

in order to mimic quantum fluctuations. In the last expression, $n_{BE,kj} = 1/(\exp(\epsilon_{k,j}/k_b T) - 1)$ is the Bose-Einstein distribution, and x_k, y_k are normally distributed Gaussian random numbers with mean zero and unit variance:

$$\begin{aligned} &\overline{\alpha_{p,j}} = \overline{\alpha_{p,j}\alpha_{q,j}} = 0, \\ &\overline{\alpha^*_{p,j}\alpha_{q,k}} = (n_{BE,pj} + 1/2)\delta_{p,q}\delta_{j,k}. \end{aligned} \tag{B.4}$$

B.2 Dimensionless units

We define a spatial discretization a_G corresponding to the spacing of the numerical grid. We define the dimensionless time $\tilde{t}$, space $\tilde{x}$ and j field $\tilde{\Psi}_j$ using the following transformations

$$z \to a_G \tilde{z}, \quad t \to \frac{\tilde{t}}{\omega_G}, \quad \Psi_j \to \frac{1}{\sqrt{a_G}}\tilde{\Psi}_j, \tag{B.5}$$

where $\omega_G = \hbar/(m a_G^2)$. Expressing Eq. (3) in˜units results in

$$i\partial_{\tilde{t}}\tilde{\Psi}_1 = \left[-\frac{1}{2}\partial^2_{\tilde{x}} + \tilde{g}|\tilde{\Psi}_1|^2\right]\tilde{\Psi}_1 - \tilde{J}\tilde{\Psi}_2, \tag{B.6}$$

with the dimensionless couplings

$$\tilde{g} = 2\frac{a_s}{a_G}\frac{\omega_\perp}{\omega_G}, \quad \tilde{J} = \frac{\omega_J}{\omega_G}, \tag{B.7}$$

using the fact that $g = 2\hbar a_s \omega_\perp$, where a_s is the s-wave scattering length and $\omega_\perp$ the frequency of the radial confinement [13]. Explicitly, the left-hand side of Eq. (3) becomes

$$i\hbar\partial_t\Psi_1 = \frac{i\hbar\omega_G}{\sqrt{a_G}}\partial_{\tilde{t}}\tilde{\Psi}_1, \tag{B.8}$$

while the right-hand side becomes

$$\left[-\frac{\hbar^2}{2m}\partial_x^2 + g\,|\Psi_1|^2\right]\Psi_1 - \hbar J\Psi_2 = \left[-\frac{1}{2}\underbrace{\frac{\hbar^2}{m a_G{}^2}}_{\hbar\omega_G}\partial_{\tilde{x}}{}^2 + \frac{g}{a_G}|\tilde{\Psi}_1|^2\right]\frac{1}{\sqrt{a_G}}\tilde{\Psi}_1 - \hbar J\frac{1}{\sqrt{a_G}}\tilde{\Psi}_2. \tag{B.9}$$

Dividing both sides by $\hbar\omega_G/\sqrt{a_G}$ leads to Eq. (B.6).

References

[1] A. Streltsov, G. Adesso and M. B. Plenio, *Colloquium: Quantum coherence as a resource*, Rev. Mod. Phys. **89**, 041003 (2017), doi:10.1103/RevModPhys.89.041003.

[2] B. Josephson, *Possible new effects in superconductive tunnelling*, Physics Letters **1**(7), 251 (1962), doi:10.1016/0031-9163(62)91369-0.

[3] A. Barone and G. Paternò, *Physics and applications of the Josephson effect*, John Wiley I& Sons, Ltd, ISBN 9783527602780, doi:10.1002/352760278X (1982).

[4] J. Javanainen, *Oscillatory exchange of atoms between traps containing Bose condensates*, Phys. Rev. Lett. **57**, 3164 (1986), doi:10.1103/PhysRevLett.57.3164.

[5] M. W. Jack, M. J. Collett and D. F. Walls, *Coherent quantum tunneling between two Bose-Einstein condensates*, Phys. Rev. A **54**, R4625 (1996), doi:10.1103/PhysRevA.54.R4625.

[6] S. Giovanazzi, A. Smerzi and S. Fantoni, *Josephson effects in dilute Bose-Einstein condensates*, Phys. Rev. Lett. **84**, 4521 (2000), doi:10.1103/PhysRevLett.84.4521.

[7] M. Albiez, R. Gati, J. Fölling, S. Hunsmann, M. Cristiani and M. K. Oberthaler, *Direct observation of tunneling and nonlinear self-trapping in a single bosonic Josephson junction*, Phys. Rev. Lett. **95**, 010402 (2005), doi:10.1103/PhysRevLett.95.010402.

[8] A. Polkovnikov, S. Sachdev and S. M. Girvin, *Non-equilibrium Gross-Pitaevskii dynamics of boson lattice models*, Phys. Rev. A **66**(5) (2002), doi:10.1103/PhysRevA.66.053607.

[9] A. Posazhennikova, M. Trujillo-Martinez and J. Kroha, *Inflationary quasiparticle creation and thermalization dynamics in coupled Bose-Einstein condensates*, Phys. Rev. Lett. **116**, 225304 (2016), doi:10.1103/PhysRevLett.116.225304.

[10] M. Trujillo-Martinez, A. Posazhennikova and J. Kroha, *Nonequilibrium Josephson oscillations in Bose-Einstein condensates without dissipation*, Phys. Rev. Lett. **103**(10) (2009), doi:10.1103/PhysRevLett.103.105302.

[11] F. S. Cataliotti, S. Burger, C. Fort, P. Maddaloni, F. Minardi, A. Trombettoni, A. Smerzi and M. Inguscio, *Josephson junction arrays with Bose-Einstein condensates*, Science **293**(5531), 843 (2001), doi:10.1126/science.1062612.

[12] R. Gati and M. K. Oberthaler, *A bosonic Josephson junction*, J. Phys. B: Atom, Mol. Phys. **40** (2007), doi:10.1088/0953-4075/40/10/R01.

[13] S. Raghavan, A. Smerzi, S. Fantoni and S. R. Shenoy, *Coherent oscillations between two weakly coupled Bose-Einstein condensates: Josephson effects, π oscillations, and macroscopic quantum self-trapping*, Phys. Rev. A **59**, 620 (1999), doi:10.1103/PhysRevA.59.620.

[14] T. Schweigler, V. Kasper, S. Erne, I. Mazets, B. Rauer, F. Cataldini, T. Langen, T. Gasenzer, J. Berges and J. Schmiedmayer, *Experimental characterization of a quantum many-body system via higher-order correlations*, Nature **545**(7654), 323 (2017), doi:10.1038/nature22310.

[15] T. Langen, R. Geiger and J. Schmiedmayer, *Ultracold atoms out of equilibrium*, Annu. Rev. Condens. Matter Phys. **6**(1), 201 (2015), doi:10.1146/annurev-conmatphys-031214-014548.

[16] Y. Shin, M. Saba, T. A. Pasquini, W. Ketterle, D. E. Pritchard and A. E. Leanhardt, *Atom interferometry with Bose-Einstein condensates in a double-well potential*, Phys. Rev. Lett. **92**, 050405 (2004), doi:10.1103/PhysRevLett.92.050405.

[17] M. Pigneur, T. Berrada, M. Bonneau, T. Schumm, E. Demler and J. Schmiedmayer, *Relaxation to a phase-locked equilibrium state in a one-dimensional bosonic Josephson junction*, Phys. Rev. Lett. **120**, 173601 (2018), doi:10.1103/PhysRevLett.120.173601.

[18] T. Betz, S. Manz, R. Bücker, T. Berrada, C. Koller, G. Kazakov, I. E. Mazets, H.-P. Stimming, A. Perrin, T. Schumm and J. Schmiedmayer, *Two-point phase correlations of a one-dimensional bosonic Josephson junction*, Phys. Rev. Lett. **106**, 020407 (2011), doi:10.1103/PhysRevLett.106.020407.

[19] I. Lovas, R. Citro, E. Demler, T. Giamarchi, M. Knap and E. Orignac, *Many-body parametric resonances in the driven sine-Gordon model*, Phys. Rev. B **106**(7), 075426 (2022), doi:10.1103/PhysRevB.106.075426.

[20] C. Neuenhahn, A. Polkovnikov and F. Marquardt, *Localized phase structures growing out of quantum fluctuations in a quench of tunnel-coupled atomic condensates*, Phys. Rev. Lett. **109**(8) (2012), doi:10.1103/PhysRevLett.109.085304.

[21] S.-W. Su, S.-C. Gou, I.-K. Liu, A. S. Bradley, O. Fialko and J. Brand, *Oscillons in coupled Bose-Einstein condensates*, Phys. Rev. A **91**, 023631 (2015), doi:10.1103/PhysRevA.91.023631.

[22] P. B. Greene, L. Kofman and A. A. Starobinsky, *Sine-Gordon parametric resonance*, Nucl. Phys. B **543**, 423 (1999), doi:10.1016/S0550-3213(99)00018-8.

[23] M. Pigneur and J. Schmiedmayer, *Analytical pendulum model for a bosonic josephson junction*, Phys. Rev. A **98**, 063632 (2018), doi:10.1103/PhysRevA.98.063632.

[24] M. R. Momme, O. O. Prikhodko and Y. M. Bidasyuk, *Dispersion relations and self-localization of quasiparticles in coupled elongated Bose-Einstein condensates*, Phys. Rev. A **102**, 043316 (2020), doi:10.1103/PhysRevA.102.043316.

[25] T. Lappe, A. Posazhennikova and J. Kroha, *Fluctuation damping of isolated, oscillating Bose-Einstein condensates*, Phys. Rev. A **98**, 023626 (2018), doi:10.1103/PhysRevA.98.023626.

[26] N. K. Whitlock and I. Bouchoule, *Relative phase fluctuations of two coupled one-dimensional condensates*, Phys. Rev. A **68**(5) (2003), doi:10.1103/PhysRevA.68.053609.

[27] I. Bouchoule, *Modulational instabilities in Josephson oscillations of elongated coupled condensates*, The European Physical Journal D **35**(1), 147–154 (2005), doi:10.1140/epjd/e2005-00091-y.

[28] S. Fölling, S. Trotzky, P. Cheinet, M. Feld, R. Saers, A. Widera, T. Müller and I. Bloch, *Direct observation of second-order atom tunnelling*, Nature **448**(7157), 1029–1032 (2007), doi:10.1038/nature06112.

[29] T. Berrada, *Outlook: Bosonic Josephson Junctions Beyond the Two-Mode Approximation*, pp. 209–218, Springer International Publishing, Cham, ISBN 978-3-319-27233-7, doi:10.1007/978-3-319-27233-7_4 (2016).

[30] M. Pigneur, *Relaxation of the Josephson Oscillations in a 1D-BJJ*, pp. 117–158, Springer International Publishing, Cham, ISBN 978-3-030-52844-7, doi:10.1007/978-3-030-52844-7_3 (2020).

[31] M. Abbarchi, A. Amo, V. G. Sala, D. D. Solnyshkov, H. Flayac, L. Ferrier, I. Sagnes, E. Galopin, A. Lemaître, G. Malpuech and J. Bloch, *Macroscopic quantum self-trapping and Josephson oscillations of exciton polaritons*, Nature Physics **9**(5), 275–279 (2013), doi:10.1038/nphys2609.

[32] T. Zhang, M. Maiwöger, F. Borselli, Y. Kuriatnikov, J. Schmiedmayer and M. Prüfer, *Squeezing oscillations in a multimode bosonic Josephson junction*, Phys. Rev. X **14**(1), 011049 (2024), doi:10.1103/PhysRevX.14.011049.

[33] R. Hipolito and A. Polkovnikov, *Breakdown of macroscopic quantum self-trapping in coupled mesoscopic one-dimensional Bose gases*, Phys. Rev. A **81**(1), 013621 (2010), doi:10.1103/PhysRevLett.116.225304.

[34] S. Backhaus, S. Pereverzev, R. W. Simmonds, A. Loshak, J. C. Davis and R. E. Packard, *Discovery of a metastable π-state in a superfluid ^{3}He weak link*, Nature **392**(6677), 687 (1998), doi:10.1038/33629.

[35] T. V. Zache, V. Kasper and J. Berges, *Inflationary preheating dynamics with two-species condensates*, Phys. Rev. A **95**(6), 063629 (2017), doi:10.1103/PhysRevA.95.063629.

[36] J. Berges and J. Serreau, *Parametric resonance in quantum field theory*, Phys. Rev. Lett. **91**, 111601 (2003), doi:10.1103/PhysRevLett.91.111601.

[37] A. Chatrchyan, K. T. Geier, M. K. Oberthaler, J. Berges and P. Hauke, *Analog cosmological reheating in an ultracold Bose gas*, Phys. Rev. A **104**(2), 023302 (2021), doi:10.1103/PhysRevA.104.023302.

[38] P. B. Blakie, A. S. Bradley, M. J. Davis, R. J. Ballagh and C. W. Gardiner, *Dynamics and statistical mechanics of ultra-cold Bose gases using c-field techniques*, Adv. Phys. **57**, 363 (2008), doi:10.1080/00018730802564254.

[39] C. J. Pethick and H. Smith, *Bose–Einstein Condensation in Dilute Gases*, Cambridge University Press, 2 edn., doi:10.1017/CBO9780511802850 (2008).

[40] T. Langen, *Non-equilibrium dynamics of one-dimensional Bose gases*, Springer, doi:10.1007/978-3-319-18564-4 (2015).

[41] A. Smerzi, S. Raghavan, S. Fantoni and S. Shenoy, *Phase oscillations in superfluid ^{3}He - B weak links*, The European Physical Journal B **24**(4), 431–435 (2001), doi:10.1007/s10051-001-8695-0.

[42] J. Braden, M. C. Johnson, H. V. Peiris, A. Pontzen and S. Weinfurtner, *Nonlinear dynamics of the cold atom analog false vacuum*, JHEP **10**, 174 (2019), doi:10.1007/JHEP10(2019)174.

[43] O. Fialko, B. Opanchuk, A. I. Sidorov, P. D. Drummond and J. Brand, *Fate of the false vacuum: towards realization with ultra-cold atoms*, EPL **110**(5), 56001 (2015), doi:10.1209/0295-5075/110/56001.

[44] G. N. Felder, L. Kofman and A. D. Linde, *Tachyonic instability and dynamics of spontaneous symmetry breaking*, Phys. Rev. D **64**, 123517 (2001), doi:10.1103/PhysRevD.64.123517.

[45] F. Borselli, M. Maiwöger, T. Zhang, P. Haslinger, V. Mukherjee, A. Negretti, S. Montangero, T. Calarco, I. Mazets, M. Bonneau and J. Schmiedmayer, *Two-particle interference with double twin-atom beams*, Phys. Rev. Lett. **126**, 083603 (2021), doi:10.1103/PhysRevLett.126.083603.

[46] N. W. McLachlan, *Theory and Application of Mathieu Functions*, Clarendon Press, Oxford (1951).

[47] A. H. Nayfeh, *Perturbation Methods*, Wiley, New York, ISBN 978-0471399179, doi:10.1002/9783527617609 (1973).

[48] I. Marino, S. Raghavan, S. Fantoni, S. R. Shenoy and A. Smerzi, *Bose-condensate tunneling dynamics: Momentum-shortened pendulum with damping*, Phys. Rev. A **60**, 487 (1999), doi:10.1103/PhysRevA.60.487.

[49] M. Olshanii, *Atomic scattering in the presence of an external confinement and a gas of impenetrable bosons*, Phys. Rev. Lett. **81**(5), 938 (1998), doi:10.1103/PhysRevLett.81.938.

[50] F. Gerbier, *Quasi-1D Bose-Einstein condensates in the dimensional crossover regime*, Europhysics Letters **66**(6), 771 (2004), doi:10.1209/epl/i2004-10035-7.

[51] P. Krüger, S. Hofferberth, I. E. Mazets, I. Lesanovsky and J. Schmiedmayer, *Weakly interacting bose gas in the one-dimensional limit*, Phys. Rev. Lett. **105**, 265302 (2010), doi:10.1103/PhysRevLett.105.265302.

[52] V. Gritsev, A. Polkovnikov and E. Demler, *Linear response theory for a pair of coupled one-dimensional condensates of interacting atoms*, Phys. Rev. B **75**(17) (2007), doi:10.1103/PhysRevB.75.174511.

[53] S.-C. Ji, T. Schweigler, M. Tajik, F. Cataldini, J. a. Sabino, F. S. Møller, S. Erne and J. Schmiedmayer, *Floquet engineering a bosonic Josephson junction*, Phys. Rev. Lett. **129**(8), 080402 (2022), doi:10.1103/PhysRevLett.129.080402.

[54] T. V. Zache, T. Schweigler, S. Erne, J. Schmiedmayer and J. Berges, *Extracting the field theory description of a quantum many-body system from experimental data*, Phys. Rev. X **10**(1), 011020 (2020), doi:10.1103/PhysRevX.10.011020.

[55] R. Ott, T. V. Zache, M. Prüfer, S. Erne, M. Tajik, H. Pichler, J. Schmiedmayer and P. Zoller, *Hamiltonian learning in quantum field theories*, (arxiv preprint) (2024), doi:10.48550/arXiv.2401.01308.

[56] A. L. Gaunt, T. F. Schmidutz, I. Gotlibovych, R. P. Smith and Z. Hadzibabic, *Bose-Einstein condensation of atoms in a uniform potential*, Physical review letters **110**(20), 200406 (2013), doi:10.1103/PhysRevLett.110.200406.

[57] M. Tajik, B. Rauer, T. Schweigler, F. Cataldini, J. ao Sabino, F. S. Møller, S.-C. Ji, I. E. Mazets and J. Schmiedmayer, *Designing arbitrary one-dimensional potentials on an atom chip*, Opt. Express **27**(23), 33474 (2019), doi:10.1364/OE.27.033474.

[58] J.-F. Mennemann, I. E. Mazets, M. Pigneur, H. P. Stimming, N. J. Mauser, J. Schmiedmayer and S. Erne, *Relaxation in an extended bosonic Josephson junction*, Phys. Rev. Res. **3**, 023197 (2021), doi:10.1103/PhysRevResearch.3.023197.

[59] L. Salasnich, A. Parola and L. Reatto, *Effective wave equations for the dynamics of cigar-shaped and disk-shaped Bose condensates*, Physical Review A **65**(4), 043614 (2002), doi:10.1103/PhysRevA.65.043614.

[60] R. Folman, P. Krüger, D. Cassettari, B. Hessmo, T. Maier and J. Schmiedmayer, *Controlling cold atoms using nanofabricated surfaces: Atom chips*, Phys. Rev. Lett. **84**, 4749 (2000), doi:10.1103/PhysRevLett.84.4749.

[61] R. Folman, P. Krüger, J. Schmiedmayer, J. Denschlag and C. Henkel, *Microscopic Atom Optics: From Wires to an Atom Chip*, In *Advances in Atomic, Molecular, and Optical Physics*, vol. 48, pp. 263–356, ISBN 012003848X, doi:10.1016/S1049-250X(02)80011-8 (2002).

[62] J. Reichel and V. Vuletic, *Atom chips*, John Wiley & Sons, ISBN 978-3-527-40755-2 (2011).

[63] S. Hofferberth, I. Lesanovsky, B. Fischer, J. Verdu and J. Schmiedmayer, *Radiofrequency-dressed-state potentials for neutral atoms*, Nature Physics **2**(10), 710 (2006), doi:10.1038/nphys420.

[64] I. Lesanovsky, T. Schumm, S. Hofferberth, L. M. Andersson, P. Krüger and J. Schmiedmayer, *Adiabatic radio-frequency potentials for the coherent manipulation of matter waves*, Phys. Rev. A **73**, 033619 (2006), doi:10.1103/PhysRevA.73.033619.

[65] I. Lesanovsky, S. Hofferberth, J. Schmiedmayer and P. Schmelcher, *Manipulation of ultracold atoms in dressed adiabatic radio-frequency potentials*, Phys. Rev. A **74**, 033619 (2006), doi:10.1103/PhysRevA.74.033619.

[66] J. Grond, J. Schmiedmayer and U. Hohenester, *Optimizing number squeezing when splitting a mesoscopic condensate*, Phys. Rev. A **79**, 021603 (2009), doi:10.1103/PhysRevA.79.021603.

[67] J. Grond, G. von Winckel, J. Schmiedmayer and U. Hohenester, *Optimal control of number squeezing in trapped Bose-Einstein condensates*, Phys. Rev. A **80**, 053625 (2009), doi:10.1103/PhysRevA.80.053625.

[68] J.-F. Mennemann, D. Matthes, R.-M. Weishäupl and T. Langen, *Optimal control of Bose–Einstein condensates in three dimensions*, New Journal of Physics **17**(11), 113027 (2015), doi:10.1088/1367-2630/17/11/113027.

[69] T. Murtadho, M. Gluza, K. Z. Arifa, S. Erne, J. Schmiedmayer and N. Ng, *Systematic analysis of relative phase extraction in one-dimensional Bose gases interferometry*, (arxiv preprint) (2024), doi:10.48550/arXiv.2403.05528.

[70] M. Gluza, T. Schweigler, B. Rauer, C. Krumnow, J. Schmiedmayer and J. Eisert, *Quantum read-out for cold atomic quantum simulators*, Communications Physics **3**(1), 12 (2020), doi:10.1038/s42005-019-0273-y.

[71] M. Prüfer, Y. Minoguchi, T. Zhang, Y. Kuriatnikov, V. Marupaka and J. Schmiedmayer, *Quantum-limited generalized measurement for tunnel-coupled condensates*, (arxiv preprint) (2024), doi:10.48550/arXiv.2408.07002.

[72] R. Bücker, A. Perrin, S. Manz, T. Betz, C. Koller, T. Plisson, J. Rottmann, T. Schumm and J. Schmiedmayer, *Single-particle-sensitive imaging of freely propagating ultracold atoms*, New J. Phys. **11**(10), 103039 (2009), doi:10.1088/1367-2630/11/10/103039.

[73] L. Asteria, H. P. Zahn, M. N. Kosch, K. Sengstock and C. Weitenberg, *Quantum gas magnifier for sub-lattice-resolved imaging of 3d quantum systems*, Nature **599**(7886), 571 (2021), doi:10.1038/s41586-021-04011-2.

[74] I. Shvarchuck, C. Buggle, D. Petrov, K. Dieckmann, M. Zielonkowski, M. Kemmann, T. Tiecke, W. Von Klitzing, G. Shlyapnikov and J. Walraven, *Bose-Einstein condensation into nonequilibrium states studied by condensate focusing*, Phys. Rev. Lett. **89**(27), 270404 (2002), doi:10.1103/PhysRevLett.89.270404.

[75] S. Gregory, S. Schiattarella, V. S. Barroso, D. I. Kaiser, A. Avgoustidis and S. Weinfurtner, *Tracing the nonlinear formation of an interfacial wave spectral cascade from one to few to many*, (arXiv preprint) doi:10.48550/arXiv.2410.08842.

[76] Y. Guo, H. Yao, S. Ramanjanappa, S. Dhar, M. Horvath, L. Pizzino, T. Giamarchi, M. Landini and H.-C. Nägerl, *Experimental observation of the 2d-1d dimensional crossover in strongly interacting ultracold bosons*, Nature Physics **20**, 934 (2024), doi:10.1038/s41567-024-02459-3.

[77] Y. Guo, H. Yao, S. Dhar, L. Pizzino, M. Horvath, T. Giamarchi, M. Landini and H.-C. Nägerl, *Cooling bosons by dimensional reduction*, (arxiv preprint) doi:10.48550/arXiv.2308.04144.

[78] L. W. Clark, A. Gaj, L. Feng and C. Chin, *Collective emission of matter-wave jets from driven Bose-Einstein condensates*, Nature **551**(7680), 356 (2017), doi:10.1038/nature24272.

[79] M. Abramowitz and I. A. Stegun, *Handbook of Mathematical Functions*, Dover Publications, New York, ISBN 978-0486612720 (1972).

[80] C. Mora and Y. Castin, *Extension of Bogoliubov theory to quasicondensates*, Phys. Rev. A **67**, 053615 (2003), doi:10.1103/PhysRevA.67.053615.

[81] J. Berges and T. Gasenzer, *Quantum versus classical statistical dynamics of an ultracold Bose gas*, Phys. Rev. A **76**, 033604 (2007), doi:10.1103/PhysRevA.76.033604.